

NAGW  
1335

(NASA-CR-192677) ACTIVE NARROW  
BAND VIBRATION ISOLATION OF  
MACHINERY NOISE FROM RESONANT  
SUBSTRUCTURES (Noise Cancellation  
Technologies) 11 p

N93-71853

Unclas

Z9/39 0153299

Cambridge, MA 02139

### Abstract

Machinery noise and vibration is an important issue in many applications, including spacecraft, aircraft, and naval vessels. A classic approach to ameliorating the effect of such disturbances is isolation at a vibration transmission bottle neck; the machinery mounts. Passive approaches are widespread, and introduce no risk of instability. Active techniques promise increased isolation performance, but introduce the risk of unstable interaction with system dynamics, particularly resonant vibrations of the machine or of the supporting structure.

This paper focuses upon a specialization of active isolation; isolation of nearly time-periodic disturbances. In this situation one can achieve significant isolation performance with minimal risk of instability. The paper demonstrates, with aid of a simple case study, that the safely achievable performance is limited by three important factors: 1) The level of passive damping present in the unmodeled resonant response of the mechanical system (supporting structure and machine). The importance of passive damping is most concisely quantified by the modal overlap; the ratio of modal bandwidth to modal spacing. 2) The pole-zero structure of the transfer function from the actuators to sensors at frequencies near the disturbance frequency. For rigid machines, the single most important parameter is machine mass relative to effective modal mass. 3) The spectral bandwidth of the offending disturbance. Slowly time-varying quasi-periodic disturbances are easiest to isolate by the techniques studied. For the case study, attention is restricted to a rigid "machine" and single axis motion. The paper develops modeling analyses, discusses sensor and actuator choices, discusses control algorithms, and presents the results of an experimental study.

### 1 Introduction

Vibration is a problem in many applications, including helicopter gearboxes at 1500 Hz [1], submarine machinery at many harmonics [2], and spacecraft momentum wheels at many harmonics with important speed changes [3]. These and other potential applications of active vibration isolation have in common three basic features that one must consider in the design of an isolation system: disturbance spectrum, characteristic

structural dynamics, and machinery mounting. The disturbance spectrum is typically broadband with "spikes" at some characteristic frequency, usually that of the shaft, and harmonics [4, 5, 6]. A typical measurement of this spectrum is shown in Fig. 1 [5]. A second feature these examples have in common is the structure to which the machine is mounted. In comparison with the machine, the structure is flexible, as it has its initial eigen-frequencies well below those of the machinery itself [4]. Below the first machine-eigen-frequency, the system can be modeled as a rigid mass attached to a flexible substructure. The final commonality of these examples is in the mounting of the machinery to the structure. Machinery mounts act as a "bottle neck" in the disturbance transmission path. This makes them attractive locations to place devices that limit disturbance transmission.

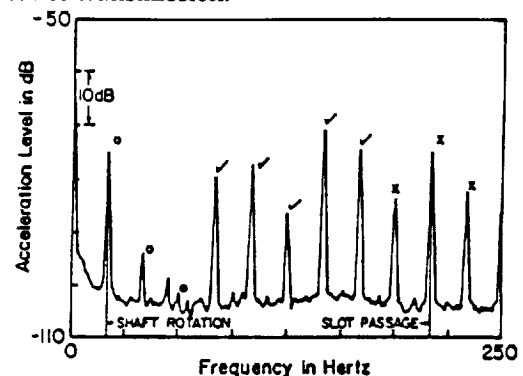


Figure 1  
Typical Machinery Spectrum

The ideal vibration isolating mount would provide stiffness to support the machine at frequencies below some performance bandwidth so that low frequency loads are transmitted. At frequencies above the bandwidth, it would be totally compliant with the assumption that vibrations at these higher frequencies are noise and should not be transmitted to (or from) the structure. This ideal stiffness function is shown in Fig. 2. Attempts to develop mounts whose stiffness functions offer a compromise to that of the ideal mount are categorized as active or passive.

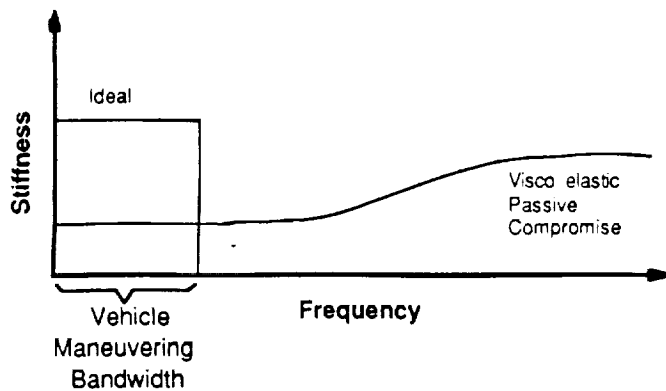


Figure 2  
Ideal Mount

### 1.1 Passive Techniques

Traditional passive devices are separated into two categories: "soft springs" and "tuned" isolators. The use of soft springs whose stiffness varies weakly with frequency (visco-elastic) or with relative deflection (non-linear) is typical. The minimum stiffness of the spring is dictated by performance requirements and clearance specifications.

"Tuned" passive isolators contain internal resonances which produce notches in the stiffness function. Every notch requires an additional degree of freedom in the mount which adds complexity, mass and occupies volume. Furthermore, mounts with internal resonances are stiffer at other frequencies. In general, passive techniques are limited by physical constraints and complexity, and cannot be readily tuned to match a time-varying machinery spectrum.

### 1.2 Active Techniques

These limitations make active control of the mount properties an attractive alternative. A feedback system may be designed to make the mount behave like the tuned or soft spring passive isolator. Additionally, more complex feedback systems can be employed with little mass or volume penalty. However, the introduction of feedback systems introduces an external energy source and therefore the possibility of instability.

Active algorithms are categorized as narrow or broad band. A broad band implementation can yield a mount with a stiffness function approximating that of the ideal mount. This is a particularly difficult task in that a detailed knowledge of the dynamic characteristics of the structure (plant) may be required to avoid the risk of unstable control-structure interaction [7]. Unfortunately, modeling errors prevent certain knowledge of the plant. Narrow band implementation yields a mount which is significantly compliant only over a small range in frequency. Here, only information of the disturbance and of general characteristics of the plant dynamics are required [4]. The resulting stiffness function is shown in Fig. 3. The "notches" in this stiffness function can be controlled to occur at the machine operating frequency and harmonics, which may vary in time.

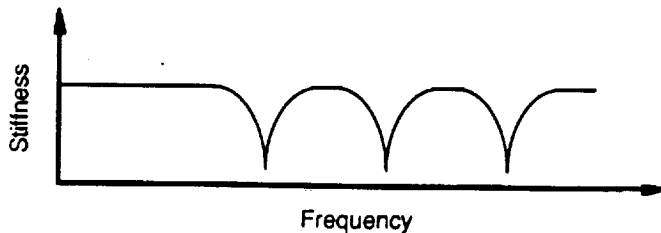


Figure 3  
Active Narrow Band Stiffness Function

This paper focuses upon such narrow band active isolation, predicting analytically the degree of performance robustly achievable in the presence of unmodeled plant resonances. The analysis quantifies the importance of passive damping, modal overlap, and pole-zero spacing. These quantities can be predicted with greater confidence than can details of the structural dynamics.

## 2 Theory

In this section the theory behind single-axis active isolation is developed. First the actuator and sensor are defined, enabling plant determination. Then compensation is presented and discussed.

### 2.1 Actuator

Given that active control has been chosen as a solution or to augment a passive system, one must decide where to place the actuator. Two basic possibilities exist: in series with the load path and in parallel with the load path (Fig. 4). If the actuator is placed parallel to some other force carrying member, it must overcome the stiffness of the force carrier to actuate. However, it does not have to bear the entire static load of the machine. If the actuator is placed directly in the load path, it must bear the load of the machine, but only has to overcome its own stiffness in actuation. Thus, stiffness and actuation authority are traded off against each other.

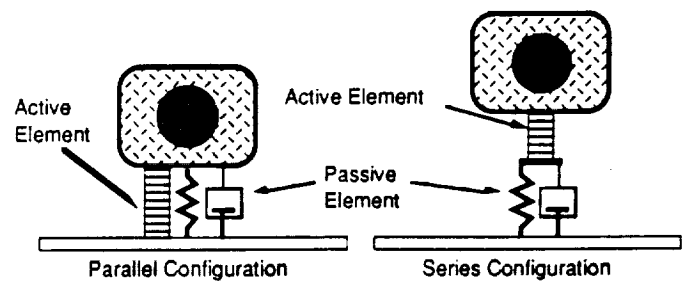


Figure 4  
Parallel and Series Mount Enhancement

Because acoustic-band disturbances are the target of this investigation, relatively high bandwidth is an actuator requirement. This inherently eases the requirements on actuation amplitude because vibration amplitude typically decreases proportional to  $\frac{1}{\omega^2}$ . In the case of machinery

noise, amplitudes on the order of fractional milli-inches can be expected in the audible bandwidth. So, the actuator requirements boil down to high bandwidth, low amplitude.

These factors point to the use of piezo-ceramic material. Often used in applications requiring bandwidths on the order of MHz, piezo-electric crystals more than meet the bandwidth criterion. Displacement in this type of device is limited by a maximum strain (about  $10^{-4} \epsilon$ ). Eq. 1 characterizes the electro-mechanical property of a one-dimensional piezo-electric material. Here, relative deflection,  $\Delta x$ , is written in terms of an applied external force,  $f$ , the displacement per voltage coefficient,  $d$ , the applied voltage,  $V$ , and the stiffness of the material,  $k$ . The piezo mass is ignored, since it is small compared to that of the machine. Refer also to Fig. 5 for a graphical illustration.

$$\Delta x = \frac{f + dV}{k} \quad (1)$$

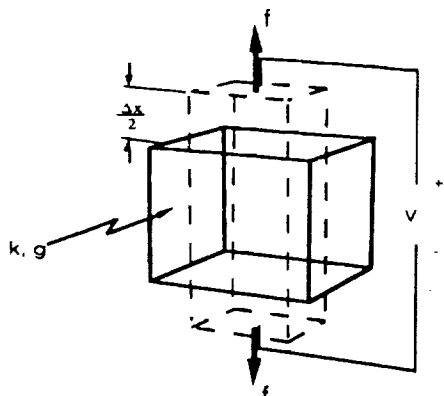


Figure 5  
Piezo-Ceramic Electro-Mechanical Coupling

The piezo-electric stacks used for this project are rated at a load-free displacement of 0.5 milli-inches, which meets the amplitude requirement. Also, with a stiffness comparable to that of aluminum, placement in series with the load path presents no major problems, although tensional loads must be avoided.

## 2.2 Sensor

With the actuator chosen, the sensor requirements can be defined. The possibilities that arise are transmitted force, relative motion, and absolute motion. Here, motion is a general category which includes acceleration, velocity, and displacement measurements. Relative motion (mount elongation) is easy to measure but not useful for isolation. Acceleration of the substructure at the mount location is a useful measurement, but sensor noise floor considerations suggest unacceptable performance limitation. Force transducers in the load path were chosen for this project.

A look at the direction of isolation offers an additional argument to sense transmitted force. Sievers [4] states that if the control loop acts to drive force between the machine and structure to zero, vibration is isolated in both directions. This is to say that machine vibrations are not transmitted to the structure and structural vibrations are not transmitted to the machine. If, on the other hand, motion is driven to zero, isolation takes place in one direction only.

## 2.3 Plant

With the actuator-sensor pair defined, the plant can be considered. Attempts at modeling the plant are prohibitive for at least two reasons. First, the structure is likely to be physically complex and a multi degree of freedom finite element model would be necessary to determine the locations of poles at high frequencies of interest. Second, as frequency increases, many assumptions that would be made in such an analysis would break down. Thus, the expected error would increase with frequency.

However, "general characteristics" of the plant are sufficient for robust narrow band control design. These general characteristics are derived in section 2.3.1. An assumption used in the derivation is that the plant model has alternating poles and zeros. The chosen sensor-actuator pair are co-located, but not dual; consequently, it cannot be assumed that the plant transfer function has alternating poles and zeros. The following discussion provides a proof showing that even though the sensor-actuator pair are not dual, the plant exhibits the necessary pole-zero pattern.

## 2.3.1 Guaranteed Properties of Flexible Structures

There are certain properties of the dynamics of any linear flexible structure that can be exploited without specifically modeling its dynamic response. A generic representation of the driving point compliance (i.e. position to force transfer function) of any structure is:

$$\frac{x(s)}{F(s)} = \frac{H \prod_{i=1}^{\infty} \left(1 - \frac{s}{z_i}\right)}{\prod_{i=1}^{\infty} \left(1 - \frac{s}{p_i}\right)} \quad (2)$$

where  $z_i$  and  $p_i$  are the complex zeros and poles, respectively, and  $H$  is a real constant.

The compliance transfer function of an undamped structure is guaranteed to have alternating poles and zeroes on the imaginary axis of the  $s$ -plane [8]; its phase alternates between  $0^\circ$  and  $-180^\circ$ . The pole-zero pattern of a damped structure is somewhat more complex. If the damping is hysteretic (complex modulus) and all materials in the structure have identical loss factors, then the poles and zeroes alternate a long a line parallel to the imaginary axis. If the damping is viscous and proportionally distributed [9], then the complex roots alternate in magnitude and the alternating pole-zero structure is preserved. If the damping is further restricted to be both proportional and modally uniform, the alternating poles and zeroes are aligned along a line in the Laplace plane. These possibilities are sketched in Fig. 6. Interesting bounds on the zero locations with respect to the pole locations are derived in Ref. [10] for SISO and MIMO structural dynamic systems.

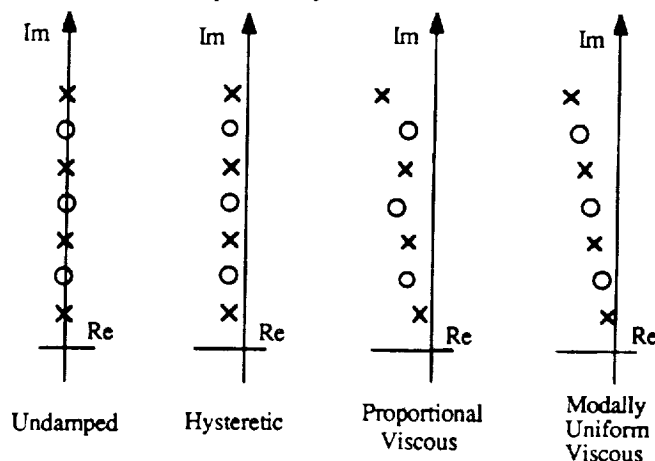


Figure 6  
Pole-Zero Patterns of Compliance for Different Damping Mechanisms

The remainder of this paper exploits a characteristic that all these patterns exhibit in the case of light damping; the pole-zero pattern of a lightly damped structure differs from that of the undamped structure only in the real part of the corresponding roots. A first-order perturbation argument [11] shows that the imaginary part is unchanged. Unfortunately, the degree to which each pole and zero is damped depends upon details of the damping mechanisms present, and upon their distribution in the structure. A typical flexible structure will have damping ratios, between .05 and .005. This corresponds to structures with roots in the region between the radial lines at  $.86^\circ$  and  $2.86^\circ$  from the complex axis of the Laplace plane. This small radial variation in pole-zero placement leads one to believe that an analysis for a system with either of the three damping mechanisms listed in Fig. 6 would show similar results.

### 2.3.2 Pole-Zero Pattern of Flexible Machine Mounted on Flexible Structure

Structural control designers normally work with sensor-actuator pairs that are dual and essentially collocated. The advantage of a dual-collocated pair is that the undamped plant transfer function is assured to have an alternating pole-zero pattern on the complex axis of the Laplace plane; its phase remains within a 180° range. This is important in structural control since other sensor-actuator configurations typically result in non-minimum phase zeroes or pole-zero patterns that don't alternate (e.g. two neighboring poles together on the complex axis with no zero in the interval connecting them); both leading to more difficult control situations.

The sensor-actuator pair considered for isolation is a force transducer that senses force of the actuator on the structure, and a piezo-actuator whose control input is voltage. The pair are collocated but not dual, therefore, there is no general result that predicts the phase characteristics of the plant transfer function. In the following analysis, it will be shown that even though the chosen sensor-actuator pair are not dual, they still exhibit the characteristic alternating pole-zero pattern of a collocated-dual pair. A force diagram describing the system is shown in Fig. 7. The equilibrium equations are:

$$F_1 = F_p \quad (3)$$

$$F_2 = -F_p \quad (4)$$

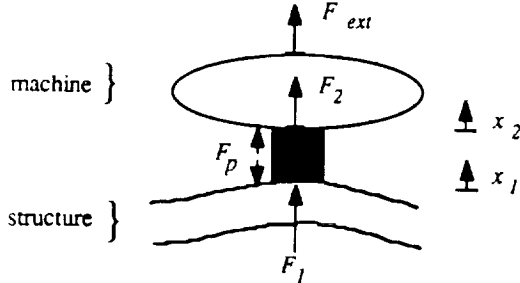


Figure 7

Force Diagram of Machine Mounted on Structure

Eqs. 5 and 6 are generic representations of the compliance transfer function at the structure-actuator interface and the machine-actuator interface, respectively.

$$\frac{x_1(s)}{F_1(s)} = \frac{H_1 \prod_{i=1}^{\infty} \left(1 - \frac{s}{z_i}\right)}{\prod_{i=1}^{\infty} \left(1 - \frac{s}{p_i}\right)} \quad (5)$$

$$\frac{x_2(s)}{F_2(s)} = \frac{H_2 \prod_{i=1}^{\infty} \left(1 - \frac{s}{z_i}\right)}{s^2 \prod_{i=1}^{\infty} \left(1 - \frac{s}{p_i}\right)} \quad (6)$$

where  $H_1$  and  $H_2$  are positive constants.

Eqs. 1, 3 and 5 can be combined to form a general expression for the plant transfer function between regulated output and controlled input:

$$\frac{F_2}{V} = \frac{s^2 \prod_{i=1}^{\infty} \left(1 - \frac{s}{p_i}\right) \prod_{j=1}^{\infty} \left(1 - \frac{s}{\bar{p}_j}\right)}{s^2 \prod_{i=1}^{\infty} \left(1 - \frac{s}{p_i}\right) \prod_{j=1}^{\infty} \left(1 - \frac{s}{\bar{p}_j}\right) + 2H_1 \prod_{i=1}^{\infty} \left(1 - \frac{s}{z_i}\right) \prod_{j=1}^{\infty} \left(1 - \frac{s}{\bar{p}_j}\right) + H_2 \prod_{i=1}^{\infty} \left(1 - \frac{s}{p_i}\right) \prod_{j=1}^{\infty} \left(1 - \frac{s}{\bar{p}_j}\right)} \quad (7)$$

The variables  $z_i$ ,  $p_i$ ,  $\bar{z}_j$ , and  $\bar{p}_j$  can be replaced by  $j\omega_{zi}$ ,  $j\omega_{pi}$ ,  $j\omega_{\bar{z}j}$ ,  $j\omega_{\bar{p}j}$ , respectively, when both the structure and machine are undamped. The relative locations of the poles and zeros can be determined since the numerator and denominator of Eq. 7 are both real. For the undamped case, the compliance transfer functions are guaranteed to have alternating pole-zero patterns, thus,  $\omega_{zi} < \omega_{pi} < \omega_{z(i+1)}$  and  $\omega_{\bar{z}i} < \omega_{\bar{p}i} < \omega_{\bar{z}(i+1)}$ . To determine the root locations, the denominator is written as a real function of  $\omega$  and set equal to zero:

$$0 = -\omega^2 \prod_{i=1}^{\infty} \left(1 - \left(\frac{\omega}{\omega_{p_i}}\right)^2\right) \prod_{j=1}^{\infty} \left(1 - \left(\frac{\omega}{\omega_{\bar{p}_j}}\right)^2\right) + \omega^2 k H_1 \prod_{i=1}^{\infty} \left(1 - \left(\frac{\omega}{\omega_{z_i}}\right)^2\right) \prod_{j=1}^{\infty} \left(1 - \left(\frac{\omega}{\omega_{\bar{p}_j}}\right)^2\right) + k H_2 \prod_{i=1}^{\infty} \left(1 - \left(\frac{\omega}{\omega_{p_i}}\right)^2\right) \prod_{j=1}^{\infty} \left(1 - \left(\frac{\omega}{\omega_{\bar{z}_j}}\right)^2\right) \quad (8)$$

The above equation can be rewritten in a more useful form for graphical solution:

$$\left( \frac{k H_2 \prod_{j=1}^{\infty} \left(1 - \left(\frac{\omega}{\omega_{\bar{z}_j}}\right)^2\right)}{\omega^2 \prod_{j=1}^{\infty} \left(1 - \left(\frac{\omega}{\omega_{\bar{p}_j}}\right)^2\right)} - 1 \right) = \frac{k H_1 \prod_{i=1}^{\infty} \left(1 - \left(\frac{\omega}{\omega_{z_i}}\right)^2\right)}{\prod_{i=1}^{\infty} \left(1 - \left(\frac{\omega}{\omega_{p_i}}\right)^2\right)} \quad (9)$$

The right hand side of Eq. 9 is the compliance transfer function of the undamped structure and is plotted in Fig. 8. The left hand side of Eq. 9 is the compliance transfer function for the undamped machine plus an additional offset factor. This function is plotted in Fig. 9, using the requirement that the values of  $\omega_{\bar{z}j}$  and  $\omega_{\bar{p}j}$  alternate with increasing frequency (i.e.  $\omega_{\bar{z}i} < \omega_{\bar{p}i} < \omega_{\bar{z}(i+1)}$ ). The roots of the plant transfer function are at the values of  $\omega$  where these two plots overlap.

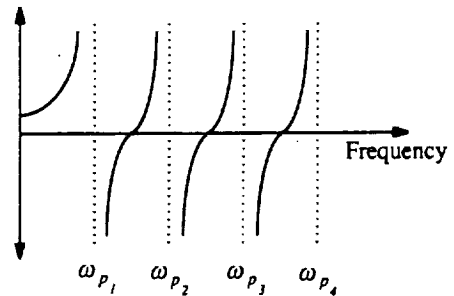


Figure 8

Right-Hand Side of Eq. 9 Plotted as a function of  $\omega$

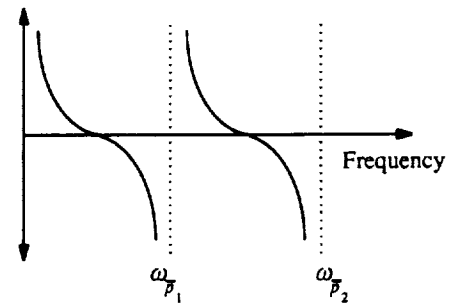


Figure 9

Left-Hand Side of Eq. 9 Plotted as a function of  $\omega$

Since the zeros of the plant transfer function occur at  $\omega_{pi}$  and  $\omega_{pi}$ , a graphical proof can easily be sketched that shows an alternating pole-zero pattern of the plant transfer function,  $\frac{y_2}{g\sqrt{V}}$ .

The preceding analysis predicts an alternating pole-zero pattern, and bounds the plant phase between  $0^\circ$  and  $180^\circ$ . The average gain trend and average phase depends upon the details of the pole-zero spacing, but are related by the Bode Gain-Phase relationship. Given that the phase is positive for all  $\omega$ , and the absence of non-minimum phase zeros, the magnitude must increase with an average slope of:

$$\left. \frac{d[20\text{Log}(\text{mag})]}{d[\text{Log}(\omega)]} \right|_{\text{Avg.}} = \frac{20\text{dB}}{\text{Decade}} \left[ \frac{\text{AvgPhase}}{90^\circ} \right] \quad (10)$$

The average slope is a function of pole-zero spacing and is bounded between zero and 40 dB/Decade. This is seen in the measured plant transfer function (Fig. 10).

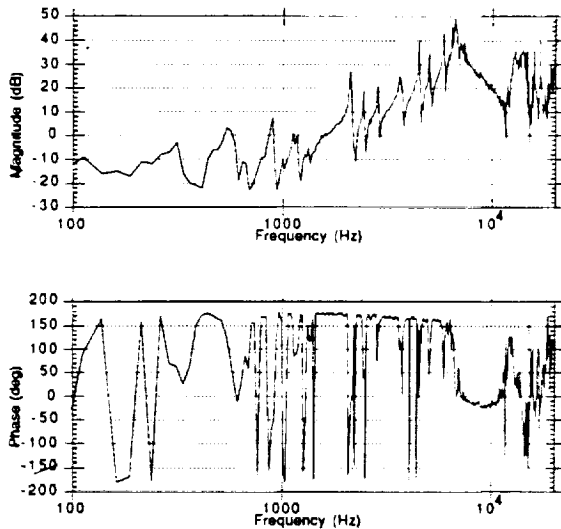


Figure 10  
Measured Plant Transfer Function

## 2.4 Compensation

Fig. 11 is a block diagram of the closed loop system. Here, the plant,  $G(s)$ , converts voltage applied to the piezo-actuator into voltage as output by the force transducer which is summed with the disturbance to produce force transmitted,  $Y(s)$ . The compensator,  $C(s)$  is fed the output of the force transducer and provides the input to the piezo-actuator. Note that the input,  $X(s)$ , to the control loop is zero, as this is the desired amount of force transmitted to the structure.

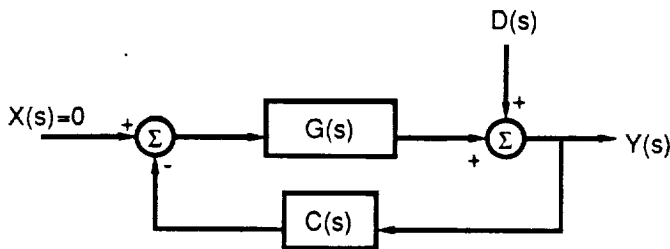


Figure 11  
Control Block Diagram

The relationship between  $D(s)$  and  $Y(s)$  is:

$$Y(s) = D(s) \frac{1}{1 + G(s)C(s)} \quad (11)$$

In order for  $D(s)$  to have a negligible influence on  $Y(s)$ , the magnitude of  $G(s)C(s)$  must be large compared to one at frequencies at which the disturbance is significant. The loop must also be stable.

For a single harmonic disturbance, a compensator consisting of a second order pole with damping ratio  $\zeta_c$  and natural frequency  $\omega_c$  satisfies these requirements. At frequencies below  $\omega_c$ , the phase of the loop function is the same as the uncompensated plant, bounded by  $+180$  and zero degrees. That the phase is so close to  $180$  degrees is not a pressing problem because phase lead errors are rarely encountered. At frequencies above  $\omega_c$ , the phase of the loop function is always greater than  $-180$  degrees. Thus, the average magnitude slope of the plant is less than 40 dB/Decade, the loop function magnitude rolls off. The phase bound of  $-180$  deg implies that the system is unconditionally stable in the absence of unmodeled phase lags.

Physical limitations of the sensor provide additional roll off. At high frequencies, the wave length of the structure approaches the length of the machinery mount footprint. Above these frequencies, the force transducer can no longer be considered a point measurement device. Instead, it acts as a distributed sensor, physically averaging load which varies over its surface. The net effect is that the transducer is incapable of passing on very high frequency load measurements. This manifests itself in the magnitude of the plant function (Fig. 10) as an abrupt roll-off without phase lag. Thus, the magnitude of the plant function does not increase without bound. This phenomenon suggests that the the size of the mount be designed as part of the control problem, and suggests the use of a distributed sensor.

## 2.5 Control-Structure Interaction

### 2.5.1 Stability Robustness

Because of the bounded property of the plant phase, phase margin can independently describe the robustness of the closed loop system. Here, phase margin is defined as the difference between the most negative excursion in phase of the loop transfer function and  $-180^\circ$ . The phase of the loop transfer function,  $G(s)C(s)$ , is the sum of the phase of the compensator,  $C(s)$ , and the phase of the plant transfer function,  $G(s)$ . Therefore, the phase margin of the loop transfer function can be divided into the sum of two parts; one contribution from plant dynamics and one contribution from compensator dynamics. This is shown graphically in Fig. 12. Here,  $PM$  is used to denote the total phase margin,  $PM_p$  to denote the phase margin contribution from the plant transfer function, and  $PM_c$  to denote the contribution from the compensator.

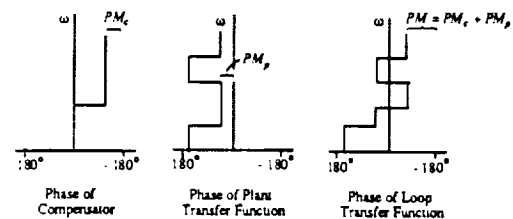


Figure 12  
Phase of Compensator, Plant, and Loop Transfer Functions

### 2.5.2 Modal and Pole-Zero Overlap

The phase margin due to the plant dynamics is a function of two variables; modal overlap,  $M$ , and pole-zero overlap,  $R$ . These quantify the similarity of high  $PM_p$ , common to plants that are heavily damped and those which exhibit modes closely spaced in frequency. Modal overlap

is defined by  $\frac{\zeta\omega_0}{\Delta\omega}$  and pole-zero overlap is defined by  $\frac{\zeta\omega_0}{\epsilon}$ ,

where  $\zeta\omega_0$  is the real part of the roots of the structure,  $\epsilon$  is zero-pole spacing, and  $\Delta\omega$  is pole-pole spacing. The phase margin determined by the contribution of only two poles and two zeroes is listed in Eq. 12.  $PM_p$  is calculated by summing up the two angles,  $\theta_1$  and  $\theta_2$  pictured in Fig. 13. This expression is valid for plants with low modal overlap.

$$PM_p = 2 \tan^{-1} \left( \frac{R - M}{RM + \frac{1}{2} \left( 1 - \frac{M}{2R} \right)} \right) \quad (12)$$

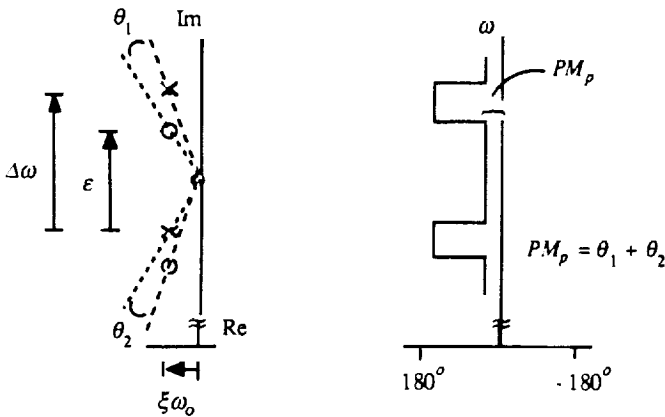


Figure 13

Phase Margin Calculated from Plant Transfer Function

For plants with higher modal overlap, contributions from more poles and zeroes are necessary for an accurate prediction of  $PM_p$ . The expression listed in Eq. 13, is valid for any value of  $M$  or  $R$ .

$$PM_p = 2 \sum_{n=0}^{n_0} \tan^{-1} \left( \frac{R - M}{RM + \frac{1}{2} \left( 1 - \frac{M}{2R} \right) + \frac{R}{M} (n + n_2)} \right) \quad (13)$$

The number of terms,  $n_0$ , necessary to get an accurate value of the Phase Margin is a linear function of modal overlap. It is calculated from the expression  $\tan(p) = \frac{M}{n_0}$ . This method for calculating  $n_0$  ignores all terms due to poles and zeroes outside a region in the Laplace plane described by the piece of pie whose borders are the lines at  $p$  radians from the positive complex axis and  $-p$  radians from the negative complex axis.

Two important results can be gathered from Eq. 13. High modal overlap implies a large phase margin. This is a very interesting and useful result since plants with high modal density are normally difficult to model accurately; consequently, model-based control designs may provide only minimal, if any, stability-robustness margins. Another factor that affects phase margin is pole-zero overlap,  $R$ . When  $R$  is large, the phase margin also increases. The plant transfer function has a much tighter bound on phase excursions when the plant has high modal or high pole-zero overlap. These two results can be restated in terms of stability-robustness. If either  $R$  or  $M$  is large, the controller can be operated with high gain since the control design is robust with respect to unknown or unmodeled plant dynamics.

Root locus provides a graphical visualization of how overlap provides stability robustness. It also sets the stage for considering the choice of compensator damping. Two systems are shown in Fig. 14: one with low overlap (system A), and one with higher overlap (system B). In this comparison, overlap is increased by (hysteretic) damping only. In both systems, a high-frequency pole is placed at  $\omega_l$  on the real axis to model lags due to amplifiers. Near and above  $\omega_l$ , the lag decreases the locus branch departure angles.

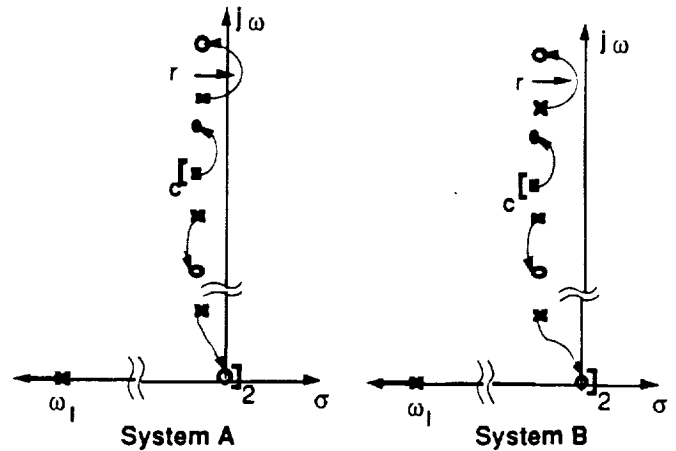


Figure 14  
Root Locus Comparison of Overlap

Because the difference in damping between the two systems does not appreciably change the shape of the locus, the approximate radius,  $r$ , the high frequency branches take on their way to associated zeros is virtually the same for both systems. Also, the gain required to move the closed loop poles to a given position on the locus is the same for both systems. However, system A has poles closer to the  $j\omega$  axis than system B. With enough modal overlap, system B has infinite gain margin. A similar graphical argument can be made if instead of increasing the damping of system B, the poles of system B are more closely spaced than in system A (assuming the poles of systems A and B have equivalent real parts). The gain required to cause instability would be greater for system B than for system A. This is due to the added stability robustness provided by the closer spaced poles.

### 2.5.3 Machine Mass and Stability Robustness

For a rigid machine, it is interesting to note how the ratio of machine mass to modal mass affects overlap and thus stability robustness [7]. If the mass of the machine is insignificant as compared to the plant modal mass, pole-zero frequency separation will approach zero. So, as machine mass approaches zero,  $R$  approaches infinity and the system gets very robust since the plant transfer function exhibits pole-zero cancellation. In this case a voltage applied to the piezo is incapable of exciting any force because it has nothing to react against; the flexible modes are uncontrollable.

On the other hand, as the mass of the machine becomes much greater than the plant modal mass, plant poles and zeros tend towards maximum separation. In the extreme of infinite machine mass, the plant transfer function becomes a measure of unloaded structural resonances. As machine mass approaches infinity,  $R$  approaches  $R_{min}$ , the unloaded plant pole-zero overlap, and robustness is minimized. In this case, plant poles occur at unloaded driving point zeros, and plant zeros occur at unloaded structural resonances.

### 2.5.4 Effects of Sensor Choice on Stability Robustness

Some interesting insights about choice of control output can be ascertained from the previous section. If position is chosen as the measured output, the alternating pole-zero pattern of the plant transfer function is still a result. The poles of the plant transfer function are the same as for the force sensing case, but the zeroes of the plant transfer function are different. The zeroes of the plant are the zeroes of the compliance functions. For the case when the machine is rigid, the factor  $R$  is smaller when force sensing is used. For at least this case, force sensing should provide a larger stability margin than position sensing. This supports the conclusion made above, that force sensing appears to be the best choice.

### 2.6 Compensator Parameters

Because no knowledge of exact frequency locations of plant poles or zeros is assumed, plant interaction with the disturbance cannot be a factor in compensator tuning. Logically, then, the natural frequency of the compensator should be tuned to the frequency of the disturbance.

Compensator damping,  $\zeta_c$ , and gain,  $K$ , then are the only parameters in question. At the disturbance frequency, higher gain implies better performance (Eq. 11). Compensator gain at  $\omega_c$  being,

$$\text{CompGain} \Big|_{\omega_c} = \frac{K}{2\zeta_c} \quad (14)$$

immediately suggests that for a given loop gain,  $K$ , best performance is realized for  $\zeta_c$  as small as possible. Stability, however, limits  $K$ . Let us assume zero damping for the compensator pole. For a plant with light damping as well, the departure angle of a loop function pole at  $\omega$  is approximately:

$$\theta_d = \underbrace{[\text{complex zeros} - \text{complex poles}]}_{\text{Below } \omega_c} ] 180^\circ - 90^\circ - \phi \quad (15)$$

Where  $\phi$  is the angle contribution from unmodeled lags

If the compensator pole is above a plant pole, its departure angle is  $90^\circ - \phi$  deg. If its damping ratio is zero, then, any finite gain sends it into the right half plane. If, on the other hand, the compensator pole is below a plant pole, its departure angle is  $-90^\circ - \phi$  deg. In this case, the plant pole causes instability and does so as a result of some finite gain. In the limit as the plant becomes well damped and plant phase approaches  $90^\circ - \phi$ , the compensator pole departure angle approaches  $-180^\circ - \phi$ , and the system is always stable. This is the simplest plant to control.

Recall that the compensator pole is tuned to some pre-determined disturbance frequency. Thus, the location of the compensator pole with respect to the plant poles is unknown. For this reason, maximum stable performance is realized with the compensator damping set to that of the plant. In this case, the pole that goes unstable cannot be distinguished as either compensator or plant, resulting in a kind of performance-stability compromise.

### 2.7 Characterization of Performance

Performance of a controller designed for isolation is defined as the attenuation achievable at the frequencies of the disturbance. Performance, like stability-robustness, is dependent on both compensator dynamics and plant dynamics.

The dependence on plant dynamics is apparent from Eq. 7. Potential performance is greatest if the disturbance frequency is close to a zero of the plant, and worst when it

is close to a pole of the plant. When damping is added to the structure, the performance is enhanced at the poles and degraded at the zeroes. Performance as a function of compensator dynamics was described by Eq. 8: high gain and low compensator damping ensures high performance.

### 3 Compensator Implementation

The desired input output relationship of this classical circuit is:

$$\frac{V_o}{V_i} = \frac{1}{s^2 + 2\zeta_p \omega_p s + \omega_p^2} \quad (16)$$

#### 3.1 Classical Implementation

This function was implemented in two ways. First, it was written in control-canonical form and assembled on a proto-board using operational amplifiers, capacitors, and resistors. In this implementation, the compensator is tuned to a predetermined disturbance frequency and is thus useless for automatic tracking of a time-varying disturbance.

#### 3.2 Self Tuning Implementation

A second, more interesting design exhibited the property of self tuning. This frequency following circuit design [12, 13, 14, 15, 16] is unique in that its transfer function is that of a second order pole whose imaginary part is set by the frequency of a reference signal pair,  $\cos(\omega t)$  and  $\sin(\omega t)$ . Fig. 15 is a block diagram of this analog algorithm.

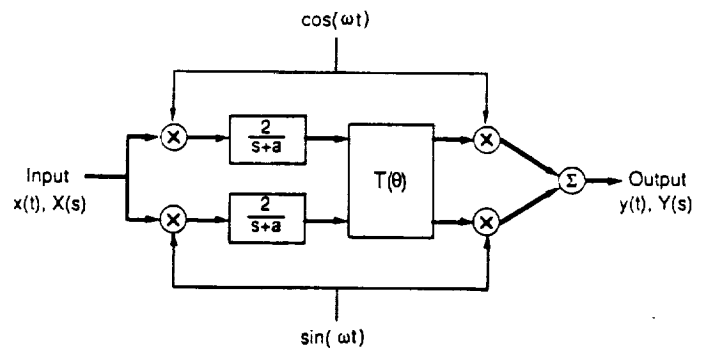


Figure 15  
Frequency Following Compensator

Here, the input on the left is multiplied by  $\sin(\omega t)$  and  $\cos(\omega t)$ . Next, the signals are low-pass filtered by a pole at  $s=-a$ . If  $a=0$ , the process becomes a sine and cosine Fourier transform at a single point in frequency space. Next, the now virtually DC signals are multiplied by a  $2 \times 2$  rotation matrix,  $T(\theta)$ . Eq. 17 shows this orthonormal matrix in terms of  $\theta$ , the angle by which  $T(\theta)$  rotates the vector:

$$T(\theta) = \begin{bmatrix} \cos(\theta) & -\sin(\theta) \\ \sin(\theta) & \cos(\theta) \end{bmatrix} \quad (17)$$

After the signals have been "rotated" in phase, they are converted back into the time domain by re-multiplication by  $\sin(\omega t)$  and  $\cos(\omega t)$  and summed, creating the output signal.

A time domain analysis offers a more rigorous and revealing description of this algorithm. The transfer function is derived using the property that the transfer function of any linear, time invariant system is the Laplace transform of the impulse response [17]:

$$\frac{Y(s)}{X(s)} = \frac{(s+a)\cos(\theta) + \omega \sin(\theta)}{(s+a)^2 + \omega^2} \quad (18)$$

which has poles and a zero at:

$$\text{Poles at } s = -a \pm j\omega$$

$$\text{Zero at } s = -[a + \omega \tan(\theta)] \quad (19)$$

The pole locations can also be expressed in terms of damping ratio and natural frequency:

$$\omega_n = \sqrt{a^2 + \omega^2} \quad (20)$$

$$\zeta_c = \frac{a}{\omega_n} \quad (21)$$

The ability of this compensator to track in frequency presents an additional facet to discuss. Tracking is very attractive in applications where the disturbance frequency changes. Even motors designed to operate at some nominal frequency will vary somewhat. Although major transient changes in frequency are not likely to occur in such motors, they can be expected in a variety of applications.

Interestingly, this compensator exhibits instantaneous response to changes in reference frequency. This is seen in Eqs 22 and 23, the response to a step in frequency applied to both the input signal and reference signal at  $t=T$  [17]. The response is separated into the steady state and transient parts.

$$y_{ss} = \frac{1}{2a} \cos(\omega t) + \frac{-\frac{a}{2} \cos(\omega t) - \omega \sin(\omega t)}{a^2 + 4\omega^2} \quad (22)$$

$$y_{tr} = \left\{ \frac{a}{8} \left( \frac{1}{\omega_1^2} - \frac{1}{\omega_2^2} \right) \cos(\eta) - \frac{1}{4} \left( \frac{1}{\omega_1} - \frac{1}{\omega_2} \right) \sin(\eta) \right\} e^{-a(t-T)}$$

where  $\eta = \omega_2(t - 2T) - \phi$  (23)

No amplitude effects are seen because the input function is restricted to be continuous. The normalized sum of Eqs. 22 and 23 is plotted in Fig. 16. Here, frequency is stepped from 1 Hz to 10 Hz, and  $a=0.1$  Hz.

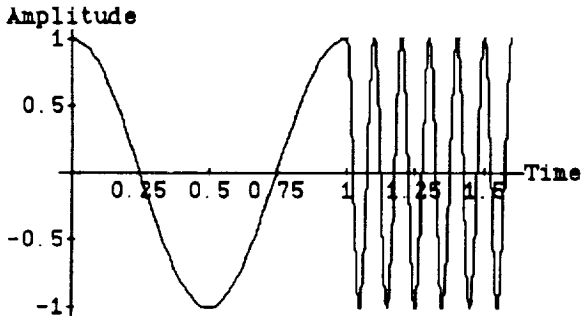


Figure 16  
Normalized Response to Step in Frequency

Note that in application, the input signal comes from a sensor, and is thus the result of filtering a disturbance through an unknown dynamic plant. The result is that the input and reference signal are unlikely to change together. Rather, the reference signal, taken from a shaft encoder, will lead the sensor signal.

#### 4 Experimental Results

Results of experimental measurements are presented in this section. The report begins with a description of the apparatus, followed by a report of the performance metric used. Next data collected using the classical controller is presented and discussed. Finally, results taken with the frequency follower as the compensator are shown.

#### 4.1 Apparatus

A cross-section of the apparatus is shown in Fig. 17. Although not shown to scale, it represents the features of the experiment. At the top is the shaker which is supported by an aluminum bracket attached to an I-beam support structure. The support structure is bolted to a cinder-block wall. The shaker is connected to the load cell via threaded rod. The load cell is fastened to the actuator assembly, which is fastened to the flexible plate. This is bolted at the corners to a 15 x 15 x 0.5 in. aluminum base plate. The base plate is bolted to the same I-beam structure as the shaker.

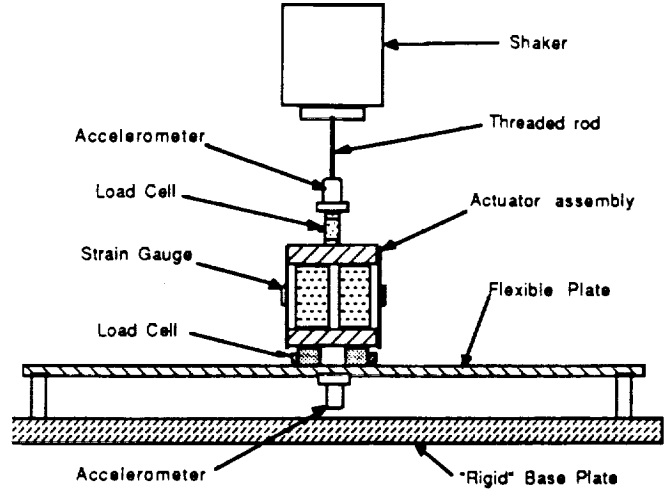


Figure 17  
Apparatus

#### 4.2 Performance Measurement

Before data can be collected, a performance metric must be chosen. Because the goal of control in this application is to reject disturbances, so that no force is transmitted to the structure by a vibrating machine, the command signal in the block diagram of Fig. 11 is zero. Comparison of transmitted force with zero conveys little information, so a transmissibility function measured under open and closed loop conditions is used to determine performance. Although the numerator of this transfer function should obviously be transmitted force, the denominator is not quite as obvious. It certainly should be a measurement of applied disturbance, either force or acceleration, so that the transfer function provides a measure of the transmitted load resulting from an application of a force or acceleration.

The choice of which metric to use depends on whether the disturbance is best modeled by a displacement or force source. The classification between disturbance sources is summarized in terms of driving point impedance of the structure at the mounting location. If the structural driving point impedance is significant compared to that of the machine, (ie the effective modal mass of the structure is significant compared the mass of the machine,  $M$ ) a force source results in a model that resembles physical reality. Otherwise, a displacement source yields a more accurate model. The assumption of a non-trivial plant implies that the driving point impedance of the structure is significant and a force source be used. However, under closed loop conditions, an active mount has the effect of reducing this impedance to the point that a displacement source would be ideal.

The solution chosen in this study is to measure both possible performance functions. Performance is determined by measuring the transfer functions between 1)



transmitted force and acceleration measured above the mount,  $P_{fa}$ , and 2) transmitted force and applied force (measured above the mount,  $P_{ff}$ . These frequency response functions are measured under open and closed loop conditions, with a spectrally white signal sent to the shaker. Finally a quantitative measurement of performance is obtained by calculating the difference between the open and closed loop magnitudes of the respective functions.

One unavoidable draw back of using these functions is that pole locations are different between  $P_{fa}$ ,  $P_{ff}$ , and the plant transfer function. Redeemingly, however, these are ideal functions for performance measurement.

#### 4.3 Classical Compensator Results

The following data were taken with the compensator natural frequency at 846 Hz and a damping ratio of 0.54%. Here, the nearest plant pole is at 877 Hz. Typical open and closed loop performance functions for this tuning are plotted in Figs. 18 and 19.

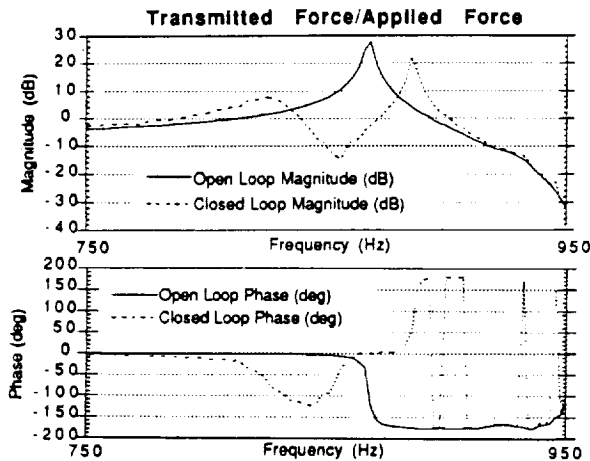


Figure 18

Typical Force Performance Function ( $\omega_c < \omega_p$ )

The closed loop data was collected with the loop gain increased so that the closed loop system was on the edge of instability. We can see from Fig. 12 that using  $P_{ff}$  as the performance metric, a maximum performance of 25 dB is achieved at the compensator natural frequency. Using  $P_{fa}$  as a performance metric (Fig. 13), a maximum performance of 22 dB is realized at the same frequency.

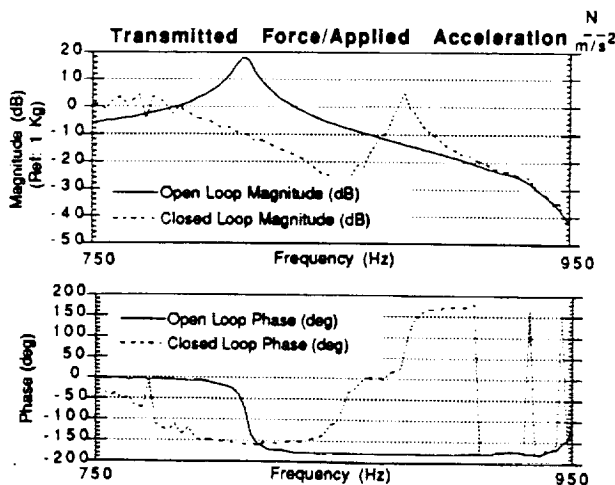


Figure 19

Typical Acceleration Performance Function ( $\omega_c < \omega_p$ )

In both performance functions, an increase in relative transmitted force is seen above and below the disturbance frequency. The closed loop transfer function has a zero at the disturbance frequency. The open loop poles move away from this closed loop zero to the neighboring open loop zeros, above and below the notch. Thus the observed increased force transmission above and below the notch result from the loop poles which move toward open loop zeros with increasing gain.

Maximum performance is plotted against compensator damping ratio in Fig. 20. Note the trend toward infinite performance for a compensator damping ratio of zero. This is because loop gain at the frequency of interest tends toward infinity for zero compensator damping. As compensator damping is increased, peak performance drops. This decrease is rapid for low damping because the rate at which the maximum gain of a second order pole decreases with respect to damping ratio is:

$$\frac{d(\text{PeakGain})}{d(\zeta_c)} = -\frac{1}{2\zeta_c^2} \quad (24)$$

Because performance is proportional to gain, it behaves similarly such that as damping ratio is increased, the decrease in performance becomes more gradual.

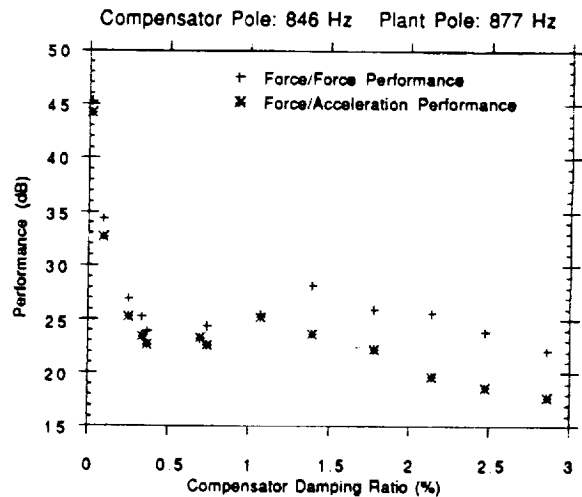


Figure 20

Performance vs Damping Ratio ( $\omega_c < \omega_p$ )

The gain at which instability occurs is plotted in Fig. 21. This plot has two distinct regions. For low compensator damping, the adjacent plant pole causes instability. As compensator damping is increased, local pole zero overlap is also increased. This is realized by the plant pole as added gain margin and appears in Fig. 21 as a greater gain required to cause instability. As the compensator pole is moved further to the left in the s-plane, it provides enough phase margin at the neighboring plant pole to prevent its instability and a new higher frequency plant pole becomes responsible for instability. The curve flattens because the incremental increase in phase margin is smaller at this higher frequency pole.

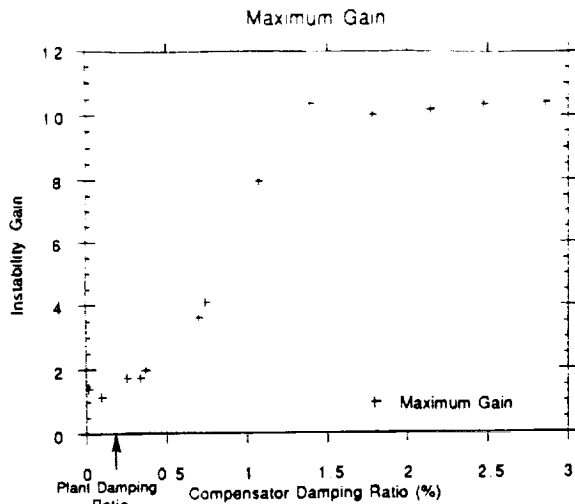


Figure 21

Maximum Gain vs. Compensator Damping Ratio ( $\omega_c < \omega_p$ )

Performance vs compensator damping for the compensator tuned to 900 Hz, which is above the plant pole, is shown in Fig. 22. With the lightly damped compensator tuned above the plant pole, performance is low. When it is close to the  $j\omega$  axis, it takes only very slight loop gain to push the compensator pole into the right half plane. As compensator damping is increased, more gain is tolerated by the closed loop system. This is realized as increasing performance in Fig. 22. When the damping is increased enough that a plant pole causes instability, the curve takes on the characteristic of decreasing performance with increasing damping ratio, similar to the curve of Fig. 14. This transition takes place at a compensator damping ratio of 0.2%, which is also the plant damping ratio. At this point, plant poles and compensator poles are equally far from the  $j\omega$  axis and require approximately the same amount of gain to move into the right half plane. As compensator damping is increased, the plant pole becomes decisively responsible for instability. This supports the stability-performance conclusion of section 2.6 that compensator damping should be set to that of the plant.

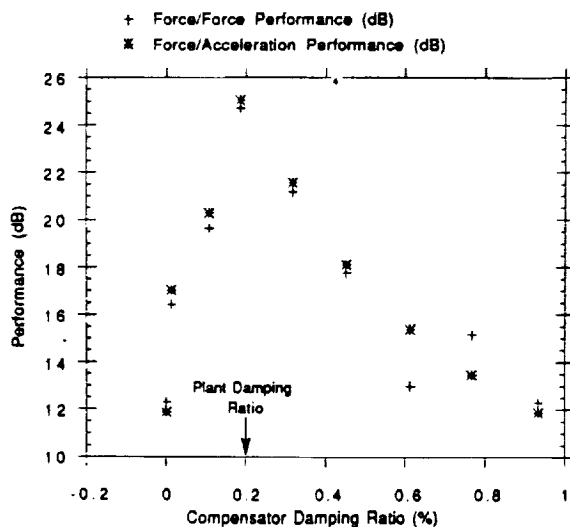


Figure 22

Performance vs Damping Ratio ( $\omega_c > \omega_p$ )

#### 4.4 Frequency Following Compensator Results

The self tuning compensator was tested for tracking performance. The real part of the conjugate poles,  $\alpha$ , of the compensator was kept constant at 9 Hz. Recall that the imaginary part of these poles is set by the frequency of a reference signal. A sinusoid with varying frequency was used as the disturbance and reference for the compensator. Frequency was increased from 800 to 1000 Hz at a rate of about 250 Hz/sec.

Open and closed loop time measurements of transmitted load are shown in Figs. 23 and 24. At  $t=0.8$  sec., where the disturbance frequency is about 877 Hz, the plant resonance at 877 Hz is clearly visible in the open loop time response. The absence of this resonance in the closed loop response indicates good performance.

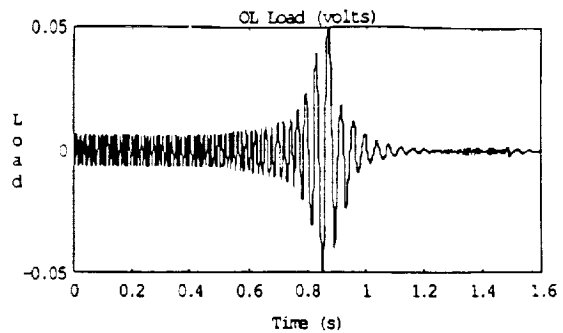


Figure 23

Open Loop Load Measurement

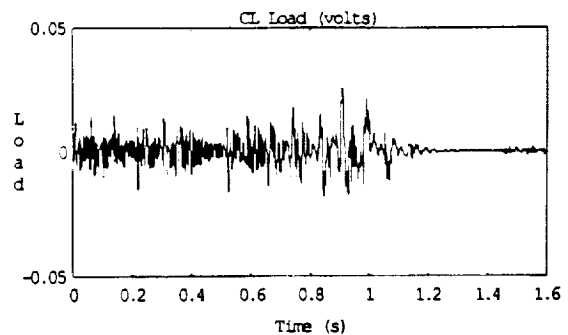


Figure 24

Closed Loop Load Measurement

The performance functions in Figs. 25 and 26 were obtained by computing  $P_{ff}$  and  $P_{fa}$  using the ramped-frequency signal as a disturbance.

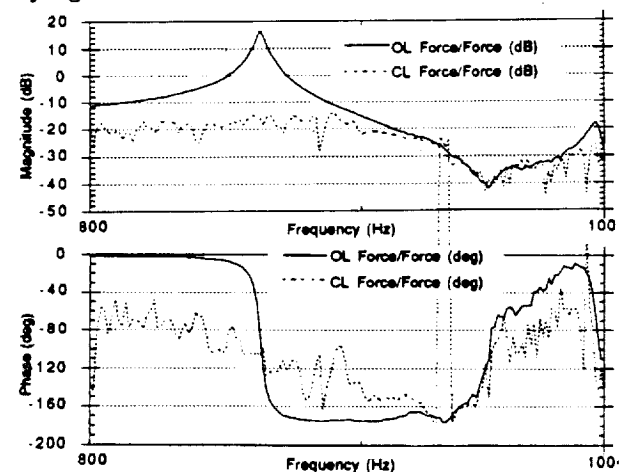


Figure 25

Open and Closed Loop  $P_{ff}$  for Ramped Frequency

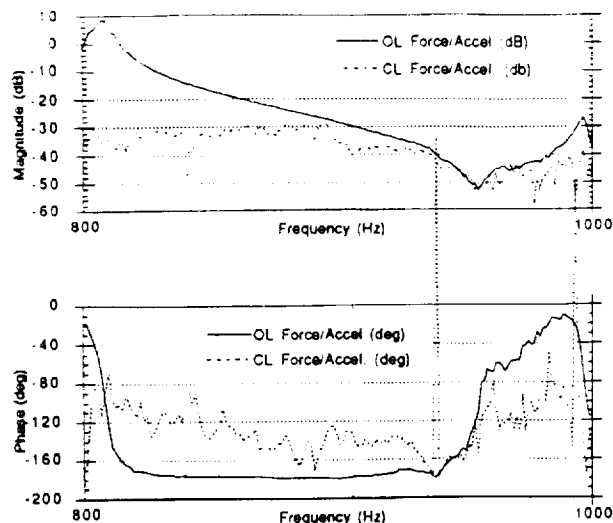


Figure 26

Open and Closed Loop  $P_{fa}$  for Ramped Frequency

### 5 Conclusions

The intent of this research was to consider active control possibilities for isolating two flexible structures from one another when the model of one or both of the structures is known with too little fidelity to permit model-based control design. The basic problem is to perform robustly stable, active narrow band isolation of a noisy machine from a flexible structure. The research resulted in a number of results applicable to different facets of structural control and vibration isolation.

Typically structural control design is done using sensor-actuator pairs that are dual and collocated. This is due to the phase bounds guaranteed for the plant transfer function. We proposed using a collocated sensor-actuator pair that is not dual. It was proven that the same phase bounds, characteristic of dual-collocated sensing and actuating, exist for the nondual pair proposed in Section 2. The resulting plant takes the form of two zeros at the origin of the s-plane, with an alternating pole-zero pattern which bounds the phase between 0 and 180°. This characteristic is guaranteed for any generic structure and machine.

Two different narrow-band compensation schemes, exploiting knowledge of the disturbance spectrum were proposed. The analysis was done assuming a very limited knowledge of plant dynamics. It was shown both theoretically and experimentally that controller performance is optimal when structure has high modal overlap -- optimal in the sense that good performance can be achieved and the controller is robust to sensor and actuator lags.

Some conclusions that can be extrapolated from this result regarding high modal overlap. It can be inferred that a structure need not have high modal overlap everywhere for guaranteed high performance. The structure needs high modal overlap only in the bandwidth of the compensator since the compensator is designed to have negligible dynamic effect at other frequencies. This property could be useful in choosing robust operating frequencies of the mounted machine. The obvious choice would be to operate in a region where modal overlap is high. This is a novel approach since typically regions of high modal overlap are avoided for state-space control design since they are difficult to model. The authors believe that these properties are applicable to more complicated systems. High modal overlap help the stability-robustness properties of broadband control schemes and other narrow band control schemes since it forces stricter bounds on the phase excursions of the plant transfer function.

### Acknowledgements

This study was performed at the Massachusetts Institute of Technology. Financial support was provided by C.S. Draper Labs, The Office of Naval Research, and NASA.

### References

- 1 Sternfeld, Harry Jr., personal communications, Boeng Helicopter, Philadelphia, PA, November, 1985
- 2 Miller, S. K., "Adaptive Filtering for Active Isolation of Machinery," MIT SM Thesis, May, 1989
- 3 Kaplow, C.E., and Velman, J.R., "Active Local Vibration Isolation Applied to a Flexible Space Telescope," Journal of Guidance and Control, May-June, 1980
- 4 Sievers, L. A. and von Flotow, A. H., "Basic Relations for Actively Isolating Structures with Unmodeled Flexibility," unpublished paper, MIT, September, 1989
- 5 Lyon, R. H., Machinery Noise and Diagnostics, Butterworth Publishers, Stoneham, MA, 1987
- 6 Eyerman, C. E., A Systems Engineering Approach to Disturbance Minimization for Spacecraft Utilizing Controlled Structures Technology, MIT SM Thesis, June, 1990.
- 7 Garcia, J. G., "Stability of an Actuated Mirror on a Flexible Structure as a Function of Mass and Structural Damping," MIT SM Thesis, June, 1990
- 8 W. B. Gevarter, Basic Relations for Control of Flexible Vehicles, AIAA Journal, vol. 8, no. 4, April 1970, pp.666-672.
- 9 L. Meirovitch, Elements of Vibration Analysis, McGraw-Hill, Inc., 1975.
- 10 T. Williams, Transmission-Zero Bounds for Large Space Structures with Applications, Journal of Guidance and Control, vol. 12, no. 1, Feb., 1989, pp. 33-38.
- 11 R. H. Plaut and K. Huseyin, Derivatives of Eigenvalues and Eigenvectors in Non-Self Adjoint Systems, AIAA Journal, vol. 11, no. 2, Feb., 1973
- 12 Glover, J.R. Jr., "Adaptive Noise Cancellation of Sinusoidal Interferences," Stanford Univ. Ph.D. Dissertation, May, 1975
- 13 Alexander, S., Private Communications, June, 1989
- 14 Hall, S. R. and Wereley, N. M., "Linear Control Issued in the Higher Harmonic Control of Helicopter Vibrations,"
- 15 Doerr, C.R., Optical Reference Gyro Characterization and Performance Enhancement, C. S. Draper Laboratory Report CSDL-T-1043, June, 1990
- 16 Elliott, S. J., Stothers, I. M., and Nelson, P. A., "A Multiple Error LMS Algorithm and Its Application to the Active Control of Sound and Vibration," *IEEE Transactions on Acoustics, Speech, and Signal Processing*, Vol ASSP-35, No. 10, October, 1987
- 17 Scribner, K. B., "Active Narrow Band Vibration Isolation of Machinery Noise from Resonant Substructures," MIT SM Thesis, Sept., 1990